Available online at www.sciencedirect.com
ScienceDirect
Trans. Nonferrous Met. Soc. China 34(2024) 2442−2454
Transactions of Nonferrous Metals Society of China
www.tnmsc.cn

Effect of cold rolling deformation on microstructure evolution and mechanical properties of spray formed Al−Zn−Mg−Cu−Cr alloys

Cai-he FAN, Yi-hui LI, Qin WU, Ling OU, Ze-yi HU, Yu-meng NI, Jian-jun YANG

College of Materials and Advanced Manufacturing, Hunan University of Technology, Zhuzhou 412007, China

Received 18 August 2023; accepted 9 April 2024

Abstract: The impact of cold rolling deformation, which was introduced after solid solution and before aging treatment, on microstructure evolution and mechanical properties of the as-extruded spray formed Al−9.8Zn−2.3Mg−1.73Cu−0.13Cr (wt.%) alloy, was investigated. SEM, TEM, and EBSD were used to analyze the microstructures, and tensile tests were conducted to assess mechanical properties. The results indicate that the D1-T6 sample, subjected to 25% cold rolling deformation, exhibits finer grains (3.35 μm) compared to the D0-T6 sample (grain size of 4.23 μm) without cold rolling. Cold rolling refines the grains that grow in solution treatment. Due to the combined effects of finer and more dispersed precipitates, higher dislocation density and smaller grains, the yield strength and ultimate tensile strength of the D1-T6 sample can reach 663 and 737 MPa, respectively. In comparison to the as-extruded and D0-T6 samples, the yield strength of the D1-T6 sample increases by 415 and 92 MPa, respectively.

Key words: Al−Zn−Mg−Cu alloy; spray forming; microstructure evolution; mechanical properties; strengthening mechanism

1 Introduction

Ultra-high-strength Al−Zn−Mg−Cu alloy (7xxx) is widely employed in aerospace, railway transportation, and various other industries due to its appealing attributes such as low density, high strength, and favorable hot workability [1−4]. Studies indicate that when the Zn content in Al−Zn−Mg−Cu alloys exceeds 8 wt.%, casting processes are prone to yield significant defects like macroscopic segregation, dendritic structures, and cracks, primarily due to slow cooling rates [5]. Nevertheless, the Zn content plays a pivotal role in enhancing the strength and toughness of 7xxx Al alloy [6,7]. By adjusting the Zn content within the range from 9 wt.% to 11 wt.%, the strength of 7xxx Al alloys can surpass 800 MPa through suitable heat treatment [8].

In comparison to conventional fabrication techniques such as casting and powder metallurgy, spray forming (SF) technology offers several advantages. It not only facilitates higher solubility of alloying elements, but also mitigates or eradicates macroscopic segregation and dendritic formation [9]. Spray-formed materials boast rapid cooling rates, uniform material structures, small grain sizes, and cost-effective production [10]. Consequently, SF stands out as an attractive and practical approach for developing high-strength Al alloys. DITTA et al [11] have produced Al−11.3Zn−2.65Mg−1Cu alloy using SF technology, and have achieved a yield strength (YS) of 807 MPa after T6 treatment. WANG et al [12] have found that the ultimate tensile strength (UTS) of spray-formed A1−10.8Zn−2.9Mg−l.9Cu alloys could attain values

Corresponding author: Qin WU, Tel: +86-731-22183467, E-mail: 420362747@qq.com
DOI: 10.1016/S1003-6326(24)66552-0

between 730 and 740 MPa, with an elongation of 8%−10% achievable through a two-stage aging treatment. Additionally, LI et al [13] have utilized SF technology to prepare Al−Zn−Mg−Cu alloys with varying Mg + Cu contents, and have revealed that samples with moderate Mg + Cu content exhibited exceptional mechanical properties following T6 treatment (UTS of 812 MPa, YS of 780 MPa, and elongation of 7.0%).

Research on SF Al alloys has predominantly centered on understanding pore formation mechanisms, designing alloy compositions, investigating thermal deformation behaviors, and optimizing subsequent heat treatment processes. However, there has been limited exploration into controlling the microstructure of SF Al alloys during heat treatment and its consequential impact on mechanical properties. Moreover, it has been widely reported that SF Al alloys exhibit uniform microstructures with minimal segregation and fine grains [14,15], but prolonged solid solution treatments may disrupt this refined microstructure. To address this, introducing suitable deformations such as extrusion, rolling, and forging can further refine the grains after solid solution treatment, ultimately optimizing the microstructure and enhancing mechanical properties. Final thermo-mechanical treatment (FTMT) is a process that combines the deformation strengthening with precipitation strengthening and is commonly employed in the production of aluminum, magnesium, and copper alloys [16,17]. CHEN et al [18] have utilized FTMT on Al−Zn−Mg−Cu alloy, and have found that mechanical properties were initially improved and then declined with increasing the pre-deformation. Additionally, LI et al [19] have found that incorporating cold rolling during the solution aging process led to 7075 alloy achieving high strength and favorable ductility.

Achieving an optimal FTMT process needs precise control of parameters such as deformation parameters, aging time, and temperatures to attain a uniform microstructure and superior performance. However, the influence of FTMT process parameters on alloy structure is relatively intricate. Existing studies have presented varying perspectives on the FTMT mechanism, particularly regarding the impact of deformation degree on final aging characteristics of alloys [20]. Therefore, in this study, we introduced cold rolling deformation after solution treatment and before aging treatment to optimize the structure and strength of the SF Al−Zn−Mg−Cu−Cr alloy. Our objective is to investigate the control of microstructure evolution and mechanical properties of SF Al−Zn−Mg−Cu−Cr alloy during the heat treatment with and without cold rolling. We examined the effect of cold rolling on the grain size, dislocation density, and precipitation characteristics of SF Al−Zn−Mg−Cu−Cr alloy during heat treatment. Lastly, we discussed the pertinent strengthening mechanisms of the cold rolling for SF Al−Zn−Mg−Cu−Cr alloy, offering theoretical guidance for industrial production.

2 Experimental

The Al−9.8Zn−2.3Mg−1.73Cu−0.13Cr (wt.%) alloy was manufactured using an SD380 spray forming equipment with proprietary intellectual property rights. Subsequently, the billet was extruded into sheets measuring 85 mm × 9 mm using a 1650 t horizontal extruder, followed by rapid water quenching. The billet and extrusion die were preheated to 460 °C for 2 h, and the extrusion barrel was preheated to 400 °C. The extrusion was conducted at a speed of 5 mm/s with an extrusion ratio of 32.5. Four test sets were prepared and designated as follows: (1) 480 °C, 90 min; (2) (480 °C, 90 min) + 25% cold rolling; (3) (480 °C, 90 min) + (120 °C, 24 h); (4) (480 °C, 90 min) + 25% cold rolling + (120 °C, 24 h), denoted as as-solutionized D0, as-solutionized D1, D0-T6, and D1-T6, respectively. Table 1 provides

Table 1 Heat treatments and deformation processes of SF Al−9.8Zn−2.3Mg−1.73Cu−0.13Cr alloy billets

Sample	Solution treatment	Deformation	Aging treatment
As-solutionized D0	480 °C, 90 min		
As-solutionized D1	480 °C, 90 min	25% cold rolling	
D0-T6	480 °C, 90 min		120 °C, 24 h
D1-T6	480 °C, 90 min	25% cold rolling	120 °C, 24 h

details of the deformation and heat treatment parameters for each set.

Microstructure analysis was carried out using an electron backscatter diffraction (EBSD) probe integrated into the SEM5000 scanning electron microscope (SEM). The acceleration voltage was set to be 20 kV, and the testing step was 0.3 μm. Data collection and analysis were performed using an Oxford Instruments Naordlys Nano EBSD system, equipped with Channel 5 data acquisition and analysis software. Precipitate characteristics were examined using an FEI Themis Z double aberration-corrected transmission electron microscope and an FEI Tecnai F30 transmission electron microscope (TEM). Composition analysis of the precipitates was conducted using energy dispersive spectrometer (EDS) and D/max 2550 X-ray diffraction (XRD). In the XRD testing, Cu K_α was utilized as the incident source with a voltage of 40 kV and current of 30 mA. The scanning range changed from 5° to 95° with a scanning step of 10 (°)/min. Tensile specimens were dimensioned in accordance with GB/T 228.1—2010 standard and were sectioned along the extrusion direction at the center of the sheet. Room temperature tensile tests were performed using the Instron 3369 universal testing machine at a rate of 1 mm/min. Each group consisted of three specimens, and the fracture morphology of the samples was subsequently observed using SEM.

3 Results

3.1 Microstructure of as-extruded sample

Figure 1(a) depicts the grain characteristics of the as-extruded Al−9.8Zn−2.3Mg−1.7Cu−0.13Cr alloy. In Fig. 1(a), the black lines represent high-angle grain boundaries (HAGBs, >15°), while the white lines represent low-angle grain boundaries (LAGBs, 2°−15°). Numerous fine, nearly equiaxed grains are evident, and some grain boundaries (GBs) appear discontinuous, as they are not fully closed. The average grain size of the alloy was determined to be 2.88 μm. In Fig. 1(b), the XRD pattern of the as-extruded sample is presented. It reveals two distinct diffraction peaks in the alloy, corresponding to the Al phase and $MgZn_2$ phase. Notably, the $MgZn_2$ phase primarily contributes to the precipitation strengthening in the as-extruded sample. The XRD pattern only exhibits two strong

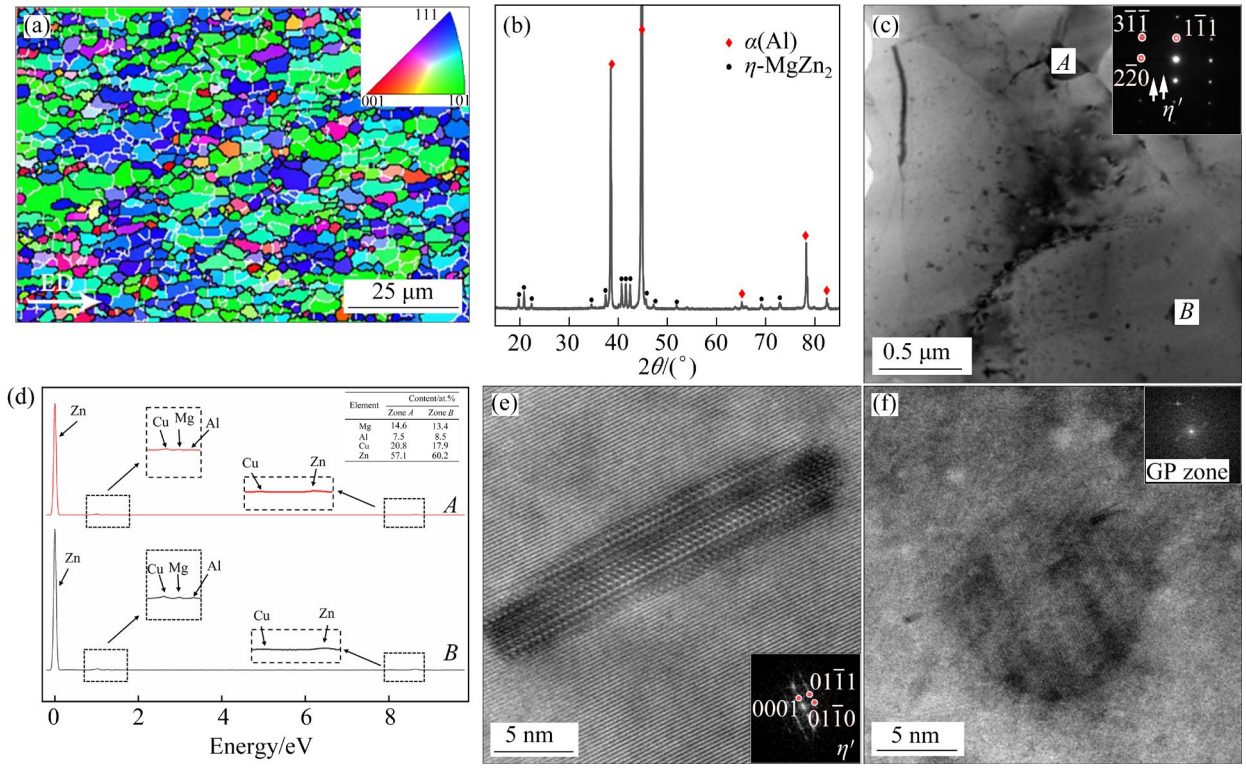

Fig. 1 Microstructure of as-extruded Al−9.8Zn−2.3Mg−1.73Cu−0.13Cr alloy: (a) Inverse pole figure; (b) XRD pattern; (c) BF TEM image; (d) EDS spectra; (e, f) HRTEM images

diffraction peaks, and it remains possible that Al_2Cu, AlZnMgCu and Al_2CuMg phases are present, albeit with weak diffraction peaks due to their low content. These phases have not been conclusively identified via XRD alone, necessitating further verification through TEM and EDS analysis.

In Fig. 1(c), the TEM image illustrates the morphology of the as-extruded alloy near the $\langle 112\rangle_{Al}$ zone axis. It is evident that dislocations are distributed unevenly within the grain, with some dislocation clusters forming dislocation wall. The precipitates exhibit notable variations in size, with the majority being small, approximately 20 nm in diameter, and a few coarser precipitates measuring around 200 nm. Coarse precipitates are also observable at the GBs. This substantial difference in precipitate size may arise from incomplete fragmentation of large second-phase particle and the concurrent precipitation of finer particles during the extrusion process. To ascertain the composition of the coarse precipitates within the grain and at the GBs (Fig. 1(d)), EDS analysis was conducted, revealing that these coarse precipitates primarily consist of Zn, Mg, and Cu alloy elements. Furthermore, the composition of precipitates at both locations is similar, indicating their identity as AlZnMgCu phases. High-resolution transmission electron microscopy (HRTEM) images were employed to further examine the crystal structure of precipitates with distinct morphologies (Figs. 1(e, f)). It is discernible that the fine precipitates within the matrix are the disc-shaped GP zone and elongated strip-shaped η' phase, consistent with previous research [21].

3.2 Microstructure evolution of alloy with and without cold rolling before aging

Figure 2 illustrates the microstructure of the alloy subjected to cold rolling deformation after solid solution and prior to aging treatment in comparison to the untreated counterpart. In the bright-field (BF) TEM images (Figs. 2(a) and (c)),

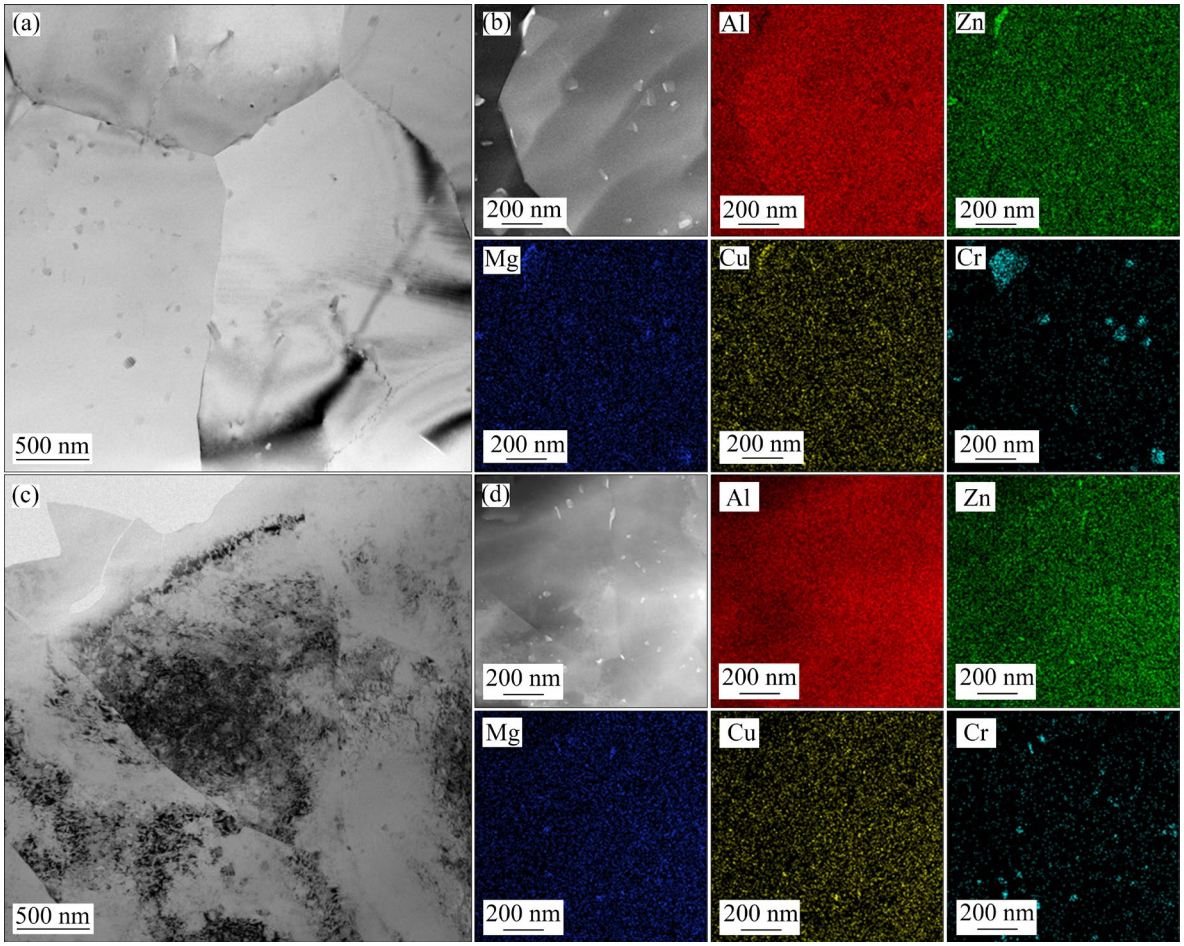

Fig. 2 Bright-field (BF) TEM images (a, c) and corresponding EDS-mappings (b, d) of alloys with and without cold rolling deformation before aging: (a, b) As-solutionized D0 sample; (c, d) As-solutionized D1 sample

it is evident that following solid solution treatment at 480 °C and 90 min, the black particles in the as-solutionlized D0 sample (Fig. 2(a)) are notably reduced when compared to those in the as-extruded sample (Fig. 1(c)). This reduction suggests that a majority of the precipitates have gradually dissolved into the Al matrix. However, some precipitates, with sizes ranging from 100 to 200 nm, remain observable, possibly indicative of the insoluble Al_7Cu_2Fe phase [22]. In contrast, the introduction of 25% cold rolling deformation in the as-solutionized D1 sample results in fragmented grains, along with a substantial number of fine dispersed precipitates with an average size of 50−100 nm (Fig. 2(c)). In addition, the as-solutionized D1 exhibits a high dislocation density, providing ample energy for subsequent aging processes. EDS-mapping analysis (Figs. 2(b) and (d)) further reveals that the precipitates in both states are rich in Zn, Mg, Cu, and Cr elements.

3.3 Microstructures of D0 and D1 samples after aging

Figures 3(a) and (d) display the grain characteristics of the T6 samples, one without and the other with cold rolling deformation (D0-T6 and D1-T6, respectively). In these images, the black lines represent high-angle grain boundaries (HAGBs, >15°), while the white lines denote low-angle grain boundaries (LAGBs, 2°−15°). In comparison to the as-extruded sample (Fig. 1(a)), the fine equiaxed grains in the D0-T6 sample (Fig. 3(a)) have grown, and the grain orientations along ⟨101⟩ and ⟨111⟩ have become more pronounced. The average grain size of the D0-T6 sample is measured to be 4.23 μm. After introducing 25% cold rolling deformation, the majority of the grains in the D1-T6 sample are elongated compared to those in the D0-T6 sample. Small grains with several micrometers in size, are dispersed around some larger grains in the D1-T6 sample (Fig. 3(d)). The cold rolling deformation in the D1-T6 sample, following solid solution treatment, introduces a significant number of dislocations. During the subsequent aging process, these dislocations undergo climbing and sliding along the sliding plane and shear zone, leading to static recovery. This process results in the formation of numerous subgrains separated by LAGBs and partial grain fragmentation in the D1-T6 sample. The grain orientation in the D1-T6 sample is more random than that in D0-T6 sample. Furthermore,

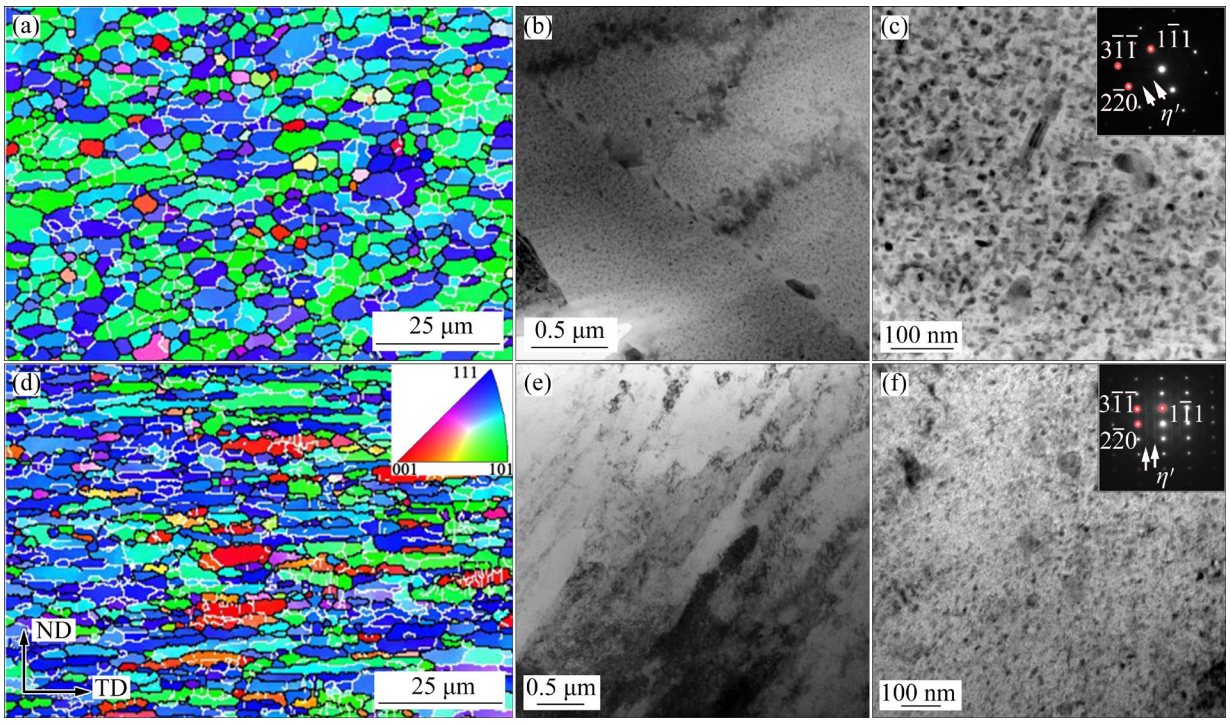

Fig. 3 Microstructures of alloys with and without cold rolling deformation after aging: (a−c) D0-T6 sample; (d−f) D1-T6 sample

the D1-T6 sample exhibits a larger grain aspect ratio and finer grain size than the D0-T6 sample, with the average grain size measuring 3.35 μm, and a reduction of 20.8% compared to that of D0-T6 sample.

Figures 3(b, c, e, f) present TEM images of the D0-T6 and D1-T6 samples near the $\langle 112\rangle_{Al}$ zone axis. In both states, numerous fine and dispersed precipitates are observed, with the D1-T6 sample exhibiting a higher dislocation density than the D0-T6 sample. Figure 3(b) reveals the TEM image of the D0-T6 sample, where a multitude of disc-shaped precipitates are distributed within the grains with sizes ranging from 5 to 15 nm. A very small number of precipitates, with a long-axis size of about 200 nm, are still observable at GBs. In comparison to the D0-T6 sample, the precipitate size, especially that at the GBs, is reduced, and the precipitate density is increased in the D1-T6 sample (Fig. 3(e)). Furthermore, the selected area electron diffraction (SAED) patterns at the upper right corner of Figs. 3(c) and (f) indicate the presence of extremely weak diffraction patterns at $1/3(2\bar{2}0)$ and $2/3(2\bar{2}0)$ of the $\langle 112\rangle_{Al}$ direction in both samples, suggesting the existence of a certain amount of η' phase. Moreover, brighter η' phase diffraction patterns are observed in the SAED of the D1-T6 sample, indicating a higher content of η' phase in the D1-T6 sample compared to that in the D0-T6 sample.

3.4 Mechanical properties

Figure 4 displays the engineering stress−strain curves for the as-extruded, D0-T6, and D1-T6 specimens. Specific values of ultimate tensile strength (UTS), yield strength (YS), and elongation (EL) for the three groups of specimens are presented in Table 2. From Fig. 4, it is evident that the performance of the as-aged samples (D0-T6 and D1-T6) is significantly improved compared to that of the as-extruded sample, regardless of the introduction of cold rolling deformation. The as-extruded sample exhibits UTS, YS, and EL values of 363 MPa, 248 MPa, and 15.7%, respectively. After solution aging treatment, the UTS of the D0-T6 samples increases by 291 MPa, YS increases by 323 MPa, while the EL decreases by 2.9% in comparison to those of the as-extruded sample. After introducing 25% cold rolling deformation, the D1-T6 specimen displays the most favorable performance, achieving UTS, YS, and EL values of 737 MPa, 663 MPa and 13.5%, respectively. In comparison to those of the D0-T6 sample, the UTS, YS, and EL of the D1-T6 specimen increase by 83 MPa, 92 MPa, and 0.7%, respectively.

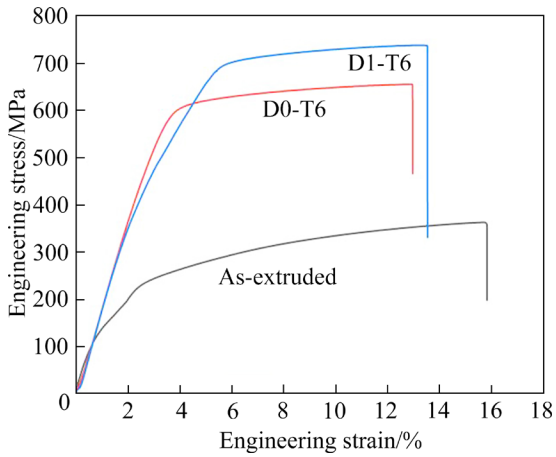

Fig. 4 Engineering stress−strain curves of SF Al−9.8Zn−2.3Mg−1.73Cu−0.13Cr alloys in different states

Table 2 Mechanical properties of SF Al−9.8Zn−2.3Mg−1.73Cu−0.13Cr alloys in different states

Sample	YS/MPa	UTS/MPa	EL/%
As-extruded	248±6	363±8	15.7±2.2
D0-T6	571±5	654±2	12.8±1.0
D1-T6	663±5	737±5	13.5±1.7

4 Discussion

Unlike the previous studies on as-extruded SF Al−Zn−Mg−Cu alloys, this study involved cold rolling deformation after solid solution and before aging treatment. The experimental findings reveal that the introduction of cold rolling deformation effectively prevents grain growth in comparison to the D0-T6 sample, thereby enhancing the material strength. The primary mechanisms underlying microstructural stability and the associated strengthening effects are discussed as follows.

4.1 Grain refinement strengthening

Figure 5 illustrates the microstructure evolution of the as-extruded, D0-T6, and D1-T6 alloys. In Figs. 5(a, d, g), grain boundary maps are presented,

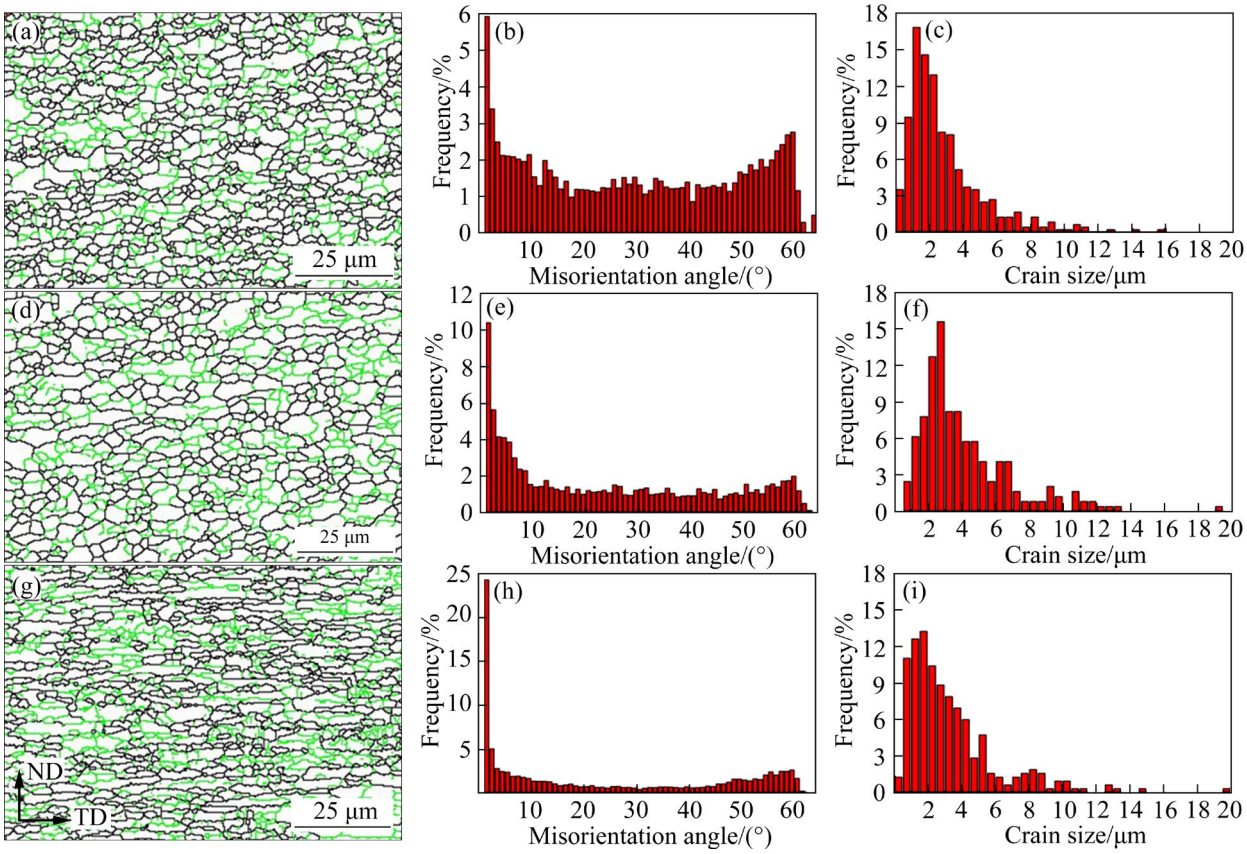

Fig. 5 Grain boundary maps (a, d, g), misorientation angle distribution histograms (b, e, h), and grain size distribution diagrams (c, f, i) of alloys in different states: (a−c) As-extruded; (d−f) D0-T6 sample; (g−i) D1-T6 sample

with black lines denoting HAGBs and green lines representing LAGBs. A more intuitive depiction is provided through misorientation angle distribution histograms in Figs. 5(b, e, h). These histograms reveal that in the as-extruded sample, HAGBs and LAGBs account for 63.5% and 36.5%, respectively. Following the T6 treatment, the proportion of HAGBs decreases to 55.37%, while the proportion of LAGBs increases to 44.63%. With the introduction of 25% cold rolling deformation, the proportions in the D1-T6 sample are 49.26% for HAGBs and 50.74% for LAGBs.

Figures 5(c, f, i) illustrate the distribution of the grain sizes. The average grain sizes for the three alloys are calculated to be 2.88, 4.23, and 3.35 μm, respectively. In the as-extruded alloy, grain sizes predominantly fall within the 0.25−4.25 μm range, accounting for 82.3% (Fig. 5(c)). In contrast, the D0-T6 alloy exhibits grain sizes concentrated in the 1.25−6.75 μm range, constituting 84.8% of the distribution (Fig. 5(f)). While the grain size distribution of the D1-T6 sample (Fig. 5(i)) resembles that of the as-extruded sample, the proportion of grain sizes within the 0.25−4.25 μm range is 78%, representing a 4% reduction compared to the as-extruded sample. Therefore, the average grain size of the D1-T6 sample is slightly larger than that of the as-extruded sample. GBs represent surface defects with various particles including supersaturated solid solution atoms and precipitates, tending to accumulate on the GB interface. Additionally, dislocations migrating to GBs can easily create blockages, impeding the dislocation movement. A finer grain size results in a larger total GB area per unit volume, thereby enhancing the strengthening effect. Numerous experimental studies have established that the contribution of GB strengthening to material strength ($\Delta\sigma_{gb}$) can be described by the Hall−Petch relationship [23]:

$$\Delta\sigma_{gb}=\sigma_0+k_y d^{-1/2} \quad (1)$$

where σ_0 is the intragranular deformation resistance, k_y is a constant used to evaluate the influence of

GBs, and d is the average grain size. Generally speaking, the smaller the d value, the higher the material strength.

During the extrusion process, the alloy undergoes substantial plastic deformation, resulting in the fragmentation of large grains and facilitating dislocation movement and recombination. This process leads to the formation of small recrystallized grains. Subsequently, during the solid solution treatment, grains tend to grow under prolonged exposure to high temperatures. However, the significant stress applied during extrusion makes a high density of dislocations generate within the grains. This, in turn, induces static recrystallization during the solid solution treatment, producing fine recrystallized grains. Hence, it is observed that in the D0-T6 sample, the original extruded grains undergo growth, although some small-sized grains can also be discerned (Fig. 5(d)). Conversely, in the D1-T6 sample, the introduction of cold rolling deformation after solid solution treatment reintroduces a significant number of dislocations. These dislocations climb and slip along slip planes and shear zones during the aging process, resulting in the fragmentation and refinement of large grains. Consequently, the grain refinement strengthening effect in the D1-T6 sample is more pronounced compared to that in the D0-T6 sample.

4.2 Dislocation strengthening

Kernel average misorientation (KAM) serves as a metric for quantifying the average value of the misalignment between a given point and its neighboring points, offering insight into grain deformation. Figure 6 illustrates the KAM diagrams and the corresponding diagrams depicting the distribution of local orientation difference angles for the as-extruded, D0-T6, and D1-T6 samples. In the KAM diagrams, the green lines can be approximated as representing the distribution of dislocations within the sample. Figures 6(a−c) reveal that the overall distribution of dislocations is uniform in all three samples. By utilizing the local misorientation distribution diagrams (Figs. 6(d−f)), the average local misorientation values for the as-extruded, D0-T6, and D1-T6 samples are calculated to be 0.39, 0.31, and 0.63 rad, respectively. Subsequently, by employing the strain theory method formula [24], the density of geometrically necessary dislocations (GNDs) (ρ_{GND}) can be quantitatively determined by

$$\rho_{GND}=2\theta/(ub) \tag{2}$$

where θ represents the average local misorientation, u represents the scanning step size of the EBSD test, and b is the amplitude of Burger vector.

By substituting all the relevant data into Eq. (2), the ρ_{GND} values for the as-extruded, D0-T6,

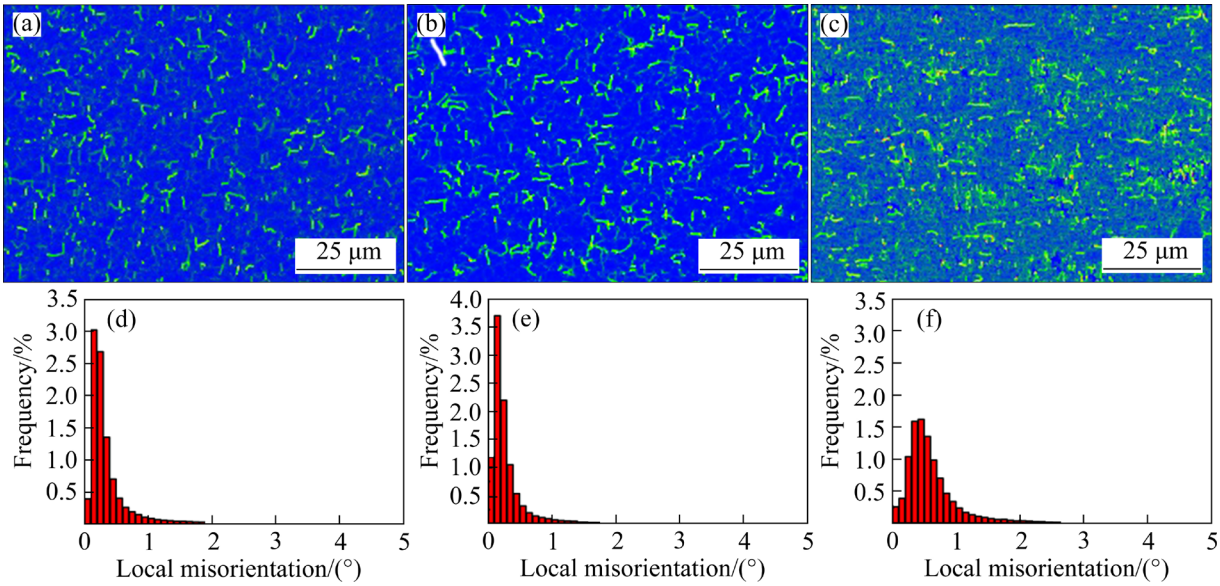

Fig. 6 KAM (a−c) and local misorientation distribution (d−f) diagrams under different conditions: (a, d) As-extruded sample; (b, e) D0-T6 sample; (c, f) D1-T6 sample

and D1-T6 specimens are computed to be 1.56×10^{14}, 1.25×10^{14}, and 2.53×10^{14} m^{-2}, respectively. In the D0-T6 sample, recovery and recrystallization processes occur during solid solution treatment, resulting in a significant reduction in high-density dislocations introduced during extrusion. Conversely, in the D1-T6 sample, the cold rolling deformation performed after solid solution treatment counteracts the reduction of dislocations during the solution treatment. Thus, the decreasing dislocation density order among the three samples is as follows: D1-T6 sample > as-extruded sample > D0-T6 sample. In accordance with the Bailey−Hirsch relationship [25], the yield strength is directly proportional to the dislocation density. Consequently, the D1-T6 sample exhibits a more pronounced dislocation strengthening effect.

4.3 Precipitation strengthening

Figure 7 presents TEM images illustrating the characteristics of precipitates in D0-T6 and D1-T6 samples. In Figs. 7(a, b), it is evident that the width of PFZs differs between the two samples. The D0-T6 sample exhibits a PFZ width of about 37.5 nm, whereas no noticeable PFZ is observed in the D1-T6 sample. Figures 7(c, d) display high-resolution transmission electron micrograph (HRTEM) images of the precipitates in the D1-T6 sample. The corresponding FFT diffractograms at the lower right corner confirm the presence of fine GP zone (Fig. 7(c)) and η' precipitates (Fig. 7(d)). Furthermore, the D1-T6 sample exhibits reduced precipitate size and increased precipitate density compared to the D0-T6 sample (Fig. 3). Consequently, precipitation strengthening effect is more pronounced in the D1-T6 sample.

Additionally, some precipitates display bright and dark morphologies (Fig. 7(e)), indicating that they consist of two or even multiple overlapping precipitates, as evidenced by the corresponding HRTEM image. FFT diffractograms reveal distinct diffraction patterns for each phase (FFT#1 and FFT#2 in Fig. 7(f)). However, the interface between the precipitates and the matrix appears blurry, suggesting the absence of an obvious orientation relationship between each precipitate and the matrix. EDS mappings (Fig. 7(g)) show that the brighter phase (FFT#1) is enriched in Zn, Mg, and Cu, while the darker phase (FFT#2) is enriched in Mg and Cr.

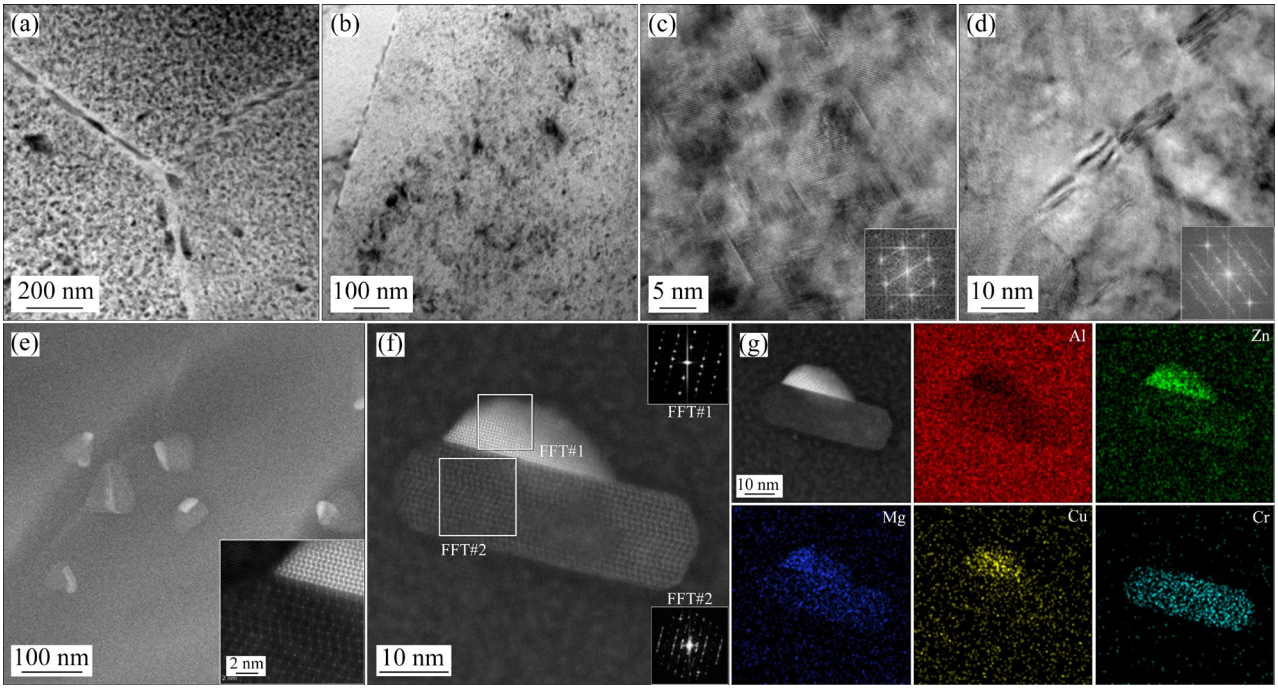

Fig. 7 TEM images showing morphology of precipitates in Al−9.8Zn−2.3Mg−1.73Cu−0.13Cr alloys after aging: BF images of D0-T6 (a) and D1-T6 (b) showing PFZ at GB; HRTEM images and corresponding FFT patterns of GP zones (c) and η' (d) in D1-T6; (e−g) STEM, HRTEM images and corresponding EDS mappings of some typical precipitates

4.4 Texture

AMIR et al [26] have investigated the effect of asymmetric cold rolling on the texture of AA7075 alloy and have found that the {011}⟨100⟩ Goss texture is strengthened, while the {112}⟨111⟩ Copper texture is weakened in the 40% asymmetric cold-rolled sample. Consequently, cold rolling deformation does influence the texture composition of Al alloys. Other studies have indicated that Al alloys can exhibit various textures during deformation, including the {001}⟨100⟩ cubic texture, Goss {011}⟨100⟩ texture, Brass {011}⟨211⟩ texture, and Copper {112}⟨111⟩ texture, among others [27]. Both deformation and solid solution treatment can induce changes in the texture characteristics. To gain a deeper understanding of the effects of different processes on the type, strength, and content of texture in the samples, the orientation distribution function (ODF) diagrams (Fig. 8) were analyzed for the as-extruded, D0-T6, and D1-T6 alloys. Figure 8(a) reveals that the texture of the as-extruded alloy primarily consists of a slightly offset rolling texture (β-fiber texture), including Brass {011}⟨211⟩, S {123}⟨634⟩, and Copper {112}⟨111⟩. Furthermore, it is observed that both D0-T6 and D1-T6 alloys (Figs. 8(b, c)) exhibit typical rolling textures similar to the as-extruded sample. However, the Cube {001}⟨100⟩ texture is exclusively present in the D1-T6 alloy (Fig. 8(c)).

4.5 Fracture mechanisms

Figure 9 displays SEM images showing the tensile fracture surfaces of SF Al−9.8Zn−2.3Mg−1.73Cu−0.13Cr alloys after T6 treatment. These surfaces exhibit fine dimples, flat cleavage surfaces, and tearing edges, indicative of typical mixed-type fracture characteristics in both D0-T6 and D1-T6 samples. Notably, the fracture surface of the D0-T6 sample appears much smoother compared to that of the D1-T6 sample. Furthermore, the dimples on the fracture surface of the D1-T6 sample are more numerous and smaller than those on the D0-T6 sample, likely attributable to the higher density of finer precipitates in the D1-T6 sample (Figs. 9(a, c)). Consequently, the mechanical properties of the D1-T6 sample surpass those of D0-T6 sample, aligning with the results observed in the tensile curves presented in Fig. 4.

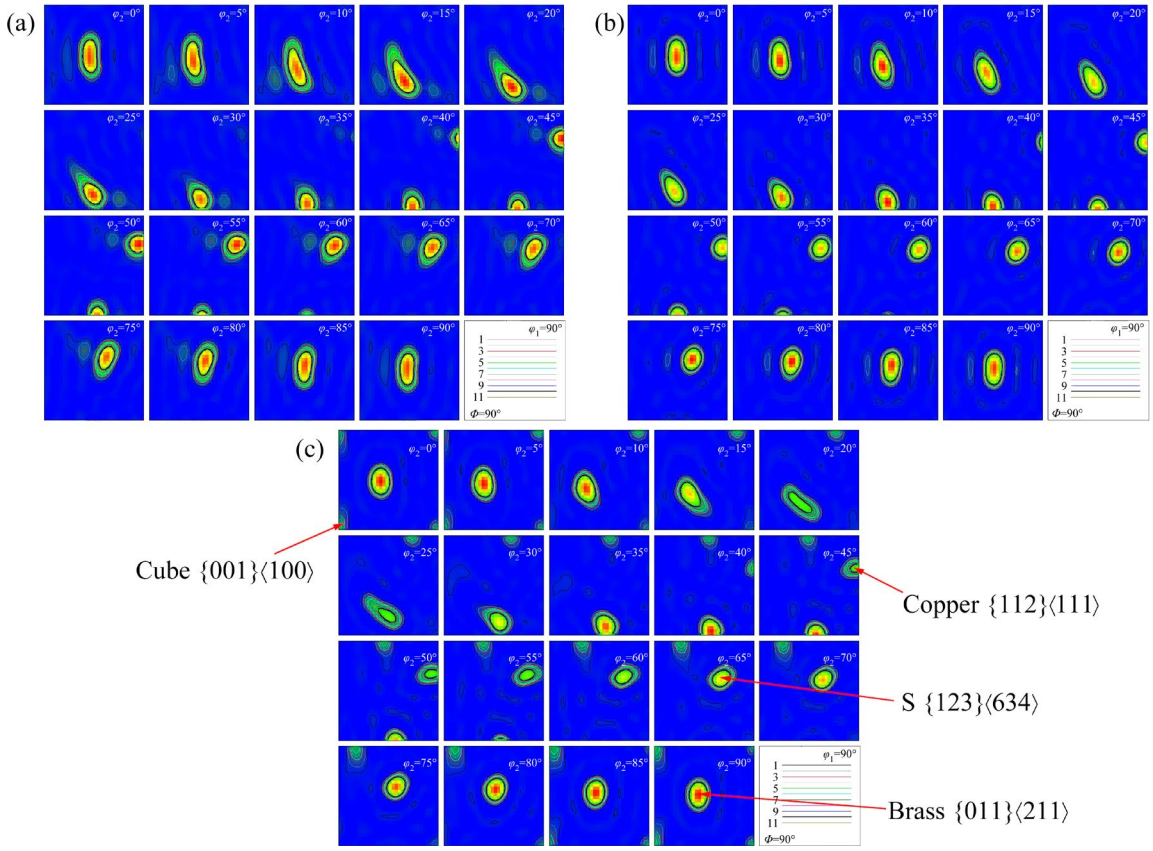

Fig. 8 ODF diagrams of as-extruded (a), D0-T6 (b) and D1-T6 (c) samples

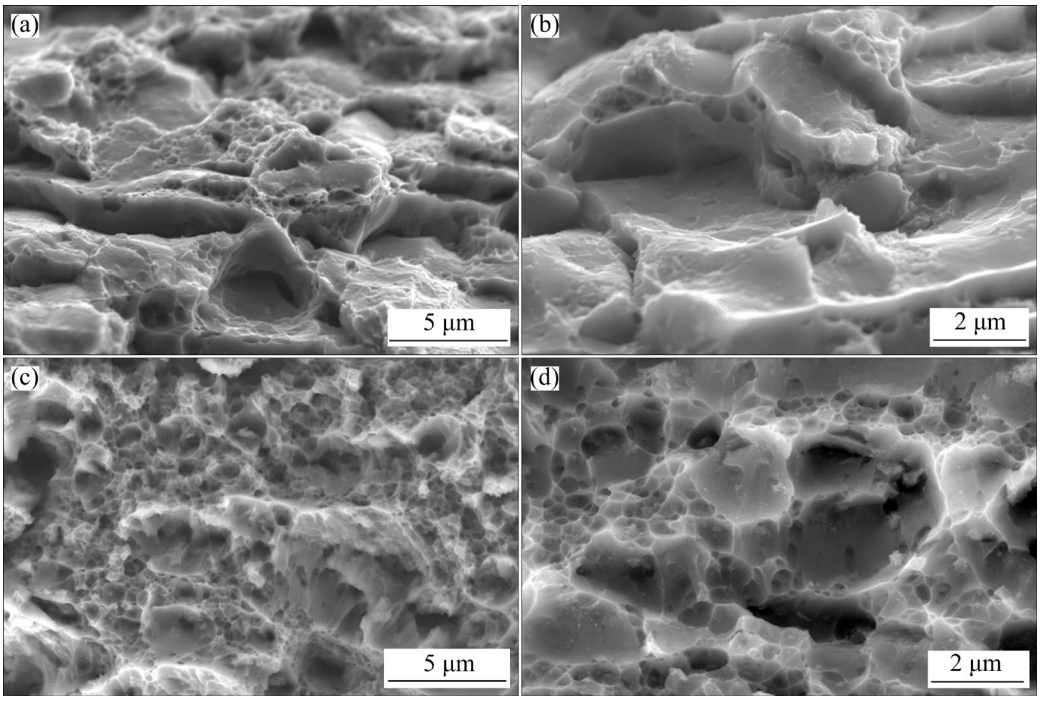

Fig. 9 SEM images showing tensile fractures of SF Al−9.8Zn−2.3Mg−1.73Cu−0.13Cr alloys: (a, b) D0-T6 sample; (c, d) D1-T6 sample

5 Conclusions

(1) The introduction of cold rolling deformation effectively refines the grains that typically grow during the solution treatment. The average grain size for the as-extruded, D0-T6, and D1-T6 samples is 2.88, 4.23 and 3.35 μm, respectively. Moreover, the cold rolling deformation indirectly optimizes precipitation during aging.

(2) Cold rolling deformation significantly enhances the strength of the as-extruded SF Al−9.8Zn−2.3Mg−1.73Cu−0.13Cr alloy, attributed to increased precipitation density, higher dislocation density, finer precipitation size, and smaller grain size. The yield strength and ultimate tensile strength of the D1-T6 sample reach 663 and 737 MPa, respectively.

CRediT authorship contribution statement

Cai-he FAN: Ideas, Formulation of overarching research goals, Acquisition of the financial support for the manuscript; **Yi-hui LI:** Data acquisition, Writing − Original draft preparation; **Qin WU:** Validation, Reviewing and editing; **Ling OU:** Data analysis; **Ze-yi HU:** Supervision; **Yu-meng NI:** Reviewing and editing; **Jian-jun YANG:** Management and coordination responsibility.

Declaration of competing interest

The authors declare that they have no known competing financial interests or personal relationships that could have appeared to influence the work reported in this paper.

Data availability

The raw/processed data required to reproduce these findings cannot be shared at this time as the data also forms part of an ongoing study.

Acknowledgments

The authors are grateful to the support from the National Natural Science Foundation of China (No. 52271177), and the Science and Technology Innovation Leaders Projects in Hunan Province, China (No. 2021RC4036).

References

[1] WANG Yi-chang, WU Xiao-dong, YUE Lu, GUO Ming-xing, CAO Ling-fei. Aging precipitation behavior and properties of Al−Zn−Mg−Cu−Zr−Er alloy at different quenching rates [J]. Transactions of Nonferrous Metals Society of China, 2022, 32(4): 1070−1082.

[2] WANG Yang, WU Rui-zhi, TURAKHODJAEV N, LIU Mei-duo. Microstructural evolution, precipitation behavior and mechanical properties of a novel Al−Zn−Mg−Cu−Li−Sc−Zr alloy [J]. Journal of Materials Research, 2021,

36(3): 740−750.

[3] JIANG Wen-ming, ZHU Jun-wen, LI Guang-yu, GUAN Feng, YU Yang, FAN Zi-tian. Enhanced mechanical properties of 6082 aluminum alloy via SiC addition combined with squeeze casting [J]. Journal of Materials Science & Technology, 2021, 88: 119−131.

[4] ZHU Jun-wen, JIANG Wen-ming, LI Guang-yu, GUAN Feng, YU Yang, FAN Zi-tian. Microstructure and mechanical properties of SiC_{np}/Al 6082 aluminum matrix composites prepared by squeeze casting combined with stir casting [J]. Journal of Materials Processing Technology, 2020, 283: 116699.

[5] LI Long, WEI Li-jun, XU Yan-jin, MAO Ling, WU Su-jun. Study on the optimizing mechanisms of superior comprehensive properties of a hot spray formed Al−Zn−Mg−Cu alloy [J]. Materials Science and Engineering A, 2019, 742: 102−108.

[6] PENG Ying-hao, LIU Chong-yu, WEI Li-li, JIANG Hong-jie, GE Zhen-jiang. Quench sensitivity and microstructures of high-Zn-content Al−Zn−Mg−Cu alloys with different Cu contents and Sc addition [J]. Transactions of Nonferrous Metals Society of China, 2021, 31(1): 24−35.

[7] YUAN Ding-ling, CHEN Song-yi, CHEN Kang-hua, HUANG Lan-ping, CHANG Jiang-yu, ZHOU Liang, DING Yun-feng. Correlations among stress corrosion cracking, grain-boundary microchemistry, and Zn content in high Zn-containing Al−Zn−Mg−Cu alloys [J]. Transactions of Nonferrous Metals Society of China, 2021, 31(8): 2220−2231.

[8] ZHANG Yong-an, ZHU Bao-hong, LIU Hong-wei, ZHANG Zhi-hui, XIONG Bai-qing, SHI Li-kai. Influence of Zn content on microstructure and properties of spray-formed 7××× series aluminum alloys [J]. The Chinese Journal of Nonferrous Metals, 2005, 15(7): 1013−1018. (in Chinese)

[9] WANG Yong-xiao, ZHAO Guo-qun, XU Xiao, CHEN Xiao-xue, ZHANG Wen-dong. Microstructures and mechanical properties of spray deposited 2195 Al−Cu−Li alloy through thermo-mechanical processing [J]. Materials Science and Engineering A, 2018, 727: 78−89.

[10] SI Chao-run, TANG Xing-ling, ZHANG Xian-jie, WANG Jun-biao. Microstructure and mechanical properties of low-pressure spray-formed Zn-rich aluminum alloy [J]. Materials Express, 2017, 7(4): 273−282.

[11] DITTA A, WEI Li-jun, XU Yan-jin, WU Su-jun. Effect of hot extrusion and optimal solution treatment on microstructure and properties of spray-formed Al−11.3Zn−2.65Mg−1Cu alloy [J]. Journal of Alloys and Compounds, 2019, 797: 558−565.

[12] WANG Zi-xing, ZHANG Yong-an, ZHU Bao-hong, LIU Hong-wei, WANG Feng, XIONG Bai-qing. Tensile and high-cycle fatigue properties of spray formed $Al_{10.8}Zn_{2.9}Mg_{1.9}Cu$ alloys after two-stage aging treatment [J]. Transactions of Nonferrous Metals Society of China, 2006, 16(4): 808−812.

[13] LI Hai-chao, CAO Fu-yang, GUO Shu, JIA Yan-dong, ZHANG Da-yue, LIU Zu-yan, WANG Pei, SCUDINO S, SUN Jian-fei. Effects of Mg and Cu on microstructures and properties of spray-deposited Al−Zn−Mg−Cu alloys [J]. Journal of Alloys and Compounds, 2017, 719: 89−96.

[14] WANG Zhi-ping, WANG Ming-liang, LI Yu-gang, XIAO Hong-yu, CHEN Han, GENG Ji-wei, LI Xian-feng, CHEN Dong, WANG Hao-wei. Effect of pretreatment on microstructural stability and mechanical property in a spray formed Al−Zn−Mg−Cu alloy [J]. Materials & Design, 2021, 203: 109618.

[15] LIU Bin, WANG Ming-pu, LEI Qian, DUAN Yu-lu, LIU Lin-xian, YU Hong-chun. Microstructure and properties of Al−Zn−Mg−Cu−Zr alloy prepared by spray deposition method [J]. The Chinese Journal of Nonferrous Metals, 2015, 25(7): 1773−1780. (in Chinese)

[16] ZHU Shi-an, LI Yao, XIANG Sheng-qian, PENG Xiao-yan, HUANG Ji-wu, XU Guo-fu. Study on microstructures and mechanical properties of Al−5.87Zn−2.07Mg−2.42Cu alloy during final thermomechanical treatment [J]. Hunan Nonferrous Metals, 2018, 34(3): 42−46. (in Chinese)

[17] ROMETSCH P A, ZHANG Y, KNIGHT S. Heat treatment of 7xxx series aluminium alloys: Some recent developments [J]. Transactions of Nonferrous Metals Society of China, 2014, 24(7): 2003−2017.

[18] CHEN Kang-hua, YANG Zhen, JIAO Hui-bin, CHEN Song-yi, CHEN Shan-da. The effect of final deformation heat treatment on the microstructure and properties of Al−Zn−Mg−Cu alloy [J]. Journal of Hunan University, 2019, 46(6): 24−30. (in Chinese)

[19] LI Hai, CHEN Peng, WANG Zhi-xiu, ZHU Fan, SONG Ren-guo, ZHENG Zi-qiao. Tensile properties, microstructures and fracture behaviors of an Al−Zn−Mg−Cu alloy during ageing after solution treating and cold-rolling [J]. Materials Science and Engineering A, 2019, 742: 798−812.

[20] ZHANG Ji-shuai, CHEN Zhi-guo, REN Jie-ke, CHEN Ji-qiang, WEI Xiang, FANG Liang. The effect of new thermal mechanical treatment on the microstructure and properties of Al−Zn−Mg−Cu alloy [J]. Transactions of Nonferrous Metals Society of China, 2015, 25(4): 910−917.

[21] HAN Nian-mei, ZHANG Xin-ming, LIU Sheng-dan, HE Dao-guang. Effect of solution treatment on the strength and fracture toughness of aluminum alloy 7050 [J]. Journal of Alloys and Compounds, 2011, 509(10): 4138−4145.

[22] ZOU Xiu-liang, YAN Hong, CHEN Xiao-hui. Evolution of second phases and mechanical properties of 7075 Al alloy processed by solution heat treatment [J]. Transactions of Nonferrous Metals Society of China, 2017, 27(10): 2146−2155.

[23] KAMIKAWA N, HUANG X X, TSUJI N, HANSEN N. Strengthening mechanisms in nanostructured high-purity aluminium deformed to high strain and annealed [J]. Acta Materialia, 2009, 57(14): 4198−4208.

[24] ZAISER M, AIFANTIS E C. Geometrically necessary dislocations and strain-gradient plasticity: A few critical issues [J]. Scripta Materialia, 2003, 48(2): 119−125.

[25] FLEISCHER R L. Substitutional solution hardening [J]. Acta Metallurgica, 1963, 11(3): 203−209.

[26] AMIR K N, ROOHOLLAH J, HAMED J A. Asymmetric cold rolling of AA7075 alloy: The evolution of microstructure, crystallographic texture, and mechanical properties [J]. Materials Science and Engineering A, 2021, 824: 141801.

[27] SIDOR J, MIROUX A, PETROV R, KESTENS L. Microstructural and crystallographic aspects of conventional and asymmetric rolling processes [J]. Acta Materialia, 2008, 56(11): 2495−2507.

冷轧变形对喷射成形 Al−Zn−Mg−Cu−Cr 合金显微组织演变及力学性能的影响

范才河，李彝会，吴 琴，欧 玲，胡泽艺，倪雨朦，阳建君

湖南工业大学 材料与先进制造学院，株洲 412007

摘 要：研究固溶后、时效前冷轧变形对喷射成形 Al−9.8Zn−2.3Mg−1.73Cu−0.13Cr (质量分数, %)挤压态合金显微组织演变及力学性能的影响。采用 SEM、TEM 和 EBSD 对合金的显微组织进行表征，并通过拉伸试验研究合金的力学性能。结果表明，与未经冷轧变形的 T6 样品(D0-T6)的晶粒尺寸(4.23 μm)相比，经 25%冷轧变形的 T6 样品(D1-T6)的晶粒尺寸减小到 3.35 μm，表明冷轧变形的引入细化了在固溶过程中长大的晶粒。由于细小弥散的析出相、高密度位错和晶粒细化的共同作用，D1-T6 样品的屈服强度和抗拉强度分别达到 663 和 737 MPa。与挤压态样品和 D0-T6 样品相比，D1-T6 样品的屈服强度分别提高了 415 和 92 MPa。

关键词：Al−Zn−Mg−Cu 合金；喷射成形；显微组织演变；力学性能；强化机理

(Edited by Wei-ping CHEN)